




Cite this: DOI: 10.1039/d4ta00473f

Functional group substitution strongly influences the performances of covalent organic frameworks in the photocatalytic metal-free oxidase reaction†

Huiying Chen, Qinghai Zhou, Jinyang Hai, Mingxiang Zhu* and Fang Zhang *

The exceptional performance of covalent organic frameworks (COFs) serving as metal-free photocatalysts has been demonstrated in numerous oxidation reactions. However, the intricate structure–activity relationship between the components, structures and reactivity of COFs remains poorly understood. This is due to their photocatalytic activity being influenced by various factors, including light absorption, charge carrier generation, separation, transport, and surface adsorption. In this study, a series of COFs with different functional group substitutions but similar topological structures were employed to investigate the relationship between the molecular structure and catalytic activity. The results reveal an activity trend in the representative superoxide radical-mediated Aza–Henry reaction, with COF-Br > COF-Cl > COF-H > COF-OMe > COF-H. Both the experimental results and density functional theory calculations confirm that the catalytic activities of COFs are closely linked to the band gap and electron affinity of the initial monomers. This study of the relationship offers a rational, time- and energy-saving strategy for developing effective COF-based photocatalysts. This approach involves evaluating the physical properties of COF monomers rather than conducting catalytic screenings on final solid COFs.

Received 21st January 2024

Accepted 27th March 2024

DOI: 10.1039/d4ta00473f

rsc.li/materials-a

Introduction

Oxidation reactions are fundamental transformations widely used in various areas, such as biological energy metabolism, organic synthetic chemistry, and environmental pollution control.¹ One specific type of oxidation reaction is called the “oxidase” reaction, wherein the oxidant contributes to catalyst turnover but does not structurally integrate into the final product.² Examples of such reactions include the oxidative Aza–Henry reaction,³ Jones oxidation,⁴ Chan–Evans–Lam coupling⁵ and the Minisci reaction.⁶ Molecular oxygen (O₂), renowned for its eco-friendly and safe characteristics, is regarded as an ideal oxidant, serving as both a proton and electron acceptor in the oxidation of organic substrates.⁷ However, it typically necessitates external energy for activation due to the stability of its spin-parallel triplet state. Currently, the activation of molecular oxygen can be accomplished through biological or chemical processes.^{8–10} In biological systems, oxidases play a key role in efficiently reducing the reaction energy barrier and the high spin transition state of oxygen under mild reaction conditions.¹¹ However, in numerous chemical oxidation processes, metal or metal oxide catalysts are frequently utilized as tools to activate oxygen.^{12–14} Considering their inherent toxicity, cost, and

requirement for demanding reaction conditions, there is a critical need for the creation and advancement of metal-free catalysts.

The activation of oxygen molecules *via* metal-free photoredox processes has become a widely esteemed approach owing to its ecological friendliness, cost-effectiveness, and sustainability. The photocatalytic activation of molecular oxygen is primarily dependent on the generation of active oxygen species (ROS), such as singlet oxygen, superoxide anion radicals, and hydroxyl radicals, through processes involving energy transfer or electron transfer facilitated by excitons (photogenerated electron–hole combinations) or photogenerated carriers induced by semiconductor photocatalysts upon illumination.¹⁵ Unmatched energy levels during catalytic processes may result in the quenching of the excited state of photocatalysts or the generation of side products incorporating oxygen by O₂ or ROS.¹⁶ Enhancing the photocatalyst’s capability to activate oxygen is crucial for achieving more effective oxidation reactions.

Covalent organic frameworks (COFs) are emerging as promising metal-free photocatalysts, with a large surface area, tunable pores, conjugated structures, and chemical stability.^{17,18} Compared to other metal-free catalysts such as carbon nitride, graphene, conjugated polymers, *etc.*, COFs offer the advantage of easy tuning of their structural composition.¹⁹ However, the rapid recombination of photo-generated carriers limits their use in photocatalytic oxidase reactions.²⁰ Enhancing the photocatalytic performance of COFs poses a significant challenge in this field. Several approaches have been developed to inhibit carrier recombination and improve activity, such as linker

Department of Chemistry, Shanghai Normal University, 100 Guilin Rd., Shanghai, 200234, China. E-mail: mingxiangzhu@shnu.edu.cn; zhangfang@shnu.edu.cn

† Electronic supplementary information (ESI) available. See DOI: <https://doi.org/10.1039/d4ta00473f>

engineering, D–A structure construction, and active guest incorporations.^{21–24} However, these approaches face difficulties in material synthesis since they require the design of appropriate building units beforehand. Instead, functional group substitution provides an effective and facile strategy for adjusting the physical and chemical properties of COFs. Specifically, introducing suitable groups into the framework, such as electron-withdrawing or electron-donating groups, offers a promising approach to alter the photocatalytic oxidation properties of materials. Despite this, there is a notable absence of investigations into the structure–property–activity relationship concerning the impact of COFs modified with diverse functional groups on photocatalytic oxidase reactions. The main reason for this gap is the heterogeneity and fuzziness of the active site composition in COF materials, which makes it challenging to identify the number, location, and properties of active sites. This difficulty, in turn, hampers the clarification of intrinsic relationships, restricting the rational development of high-performance COF-based photocatalysts.

Inspired by molecular engineering, COF materials with the same topological structure were selected to explore the structure–property–activity relationship of COF-based photocatalysts. By systematically changing the substituents R (R = OMe, OH, H, Br, Cl) of TTA-COF-R (TTA = 4,4',4''-(1,3,5-triazine-2,4,6-triyl)trianiline), the yield of a typical Aza–Henry oxidase reaction was correspondingly altered (from 10% to 79%). To validate the substituent effect, TTA was replaced by TAPB (1,3,5-tris(4-aminophenyl)benzene) to test the reactivities, which yielded consistent results, COF-Br > COF-Cl > COF-H > COF-OMe > COF-OH. Comprehensive characterization and analysis indicated that the oxidative capacity is determined using both the energy band structure and electron affinity of the initial monomers concurrently.

Results and discussion

Synthesis and characterization of COFs

To investigate the substituent effect on the properties of imine-based COFs and their photocatalytic oxidase-like activity, 5 kinds of TTA-COF-R were synthesized by the Schiff-base condensation reaction between amine monomer 4,4',4''-(1,3,5-triazine-2,4,6-triyl)trianiline (TTA) with five kinds of functionalized C₂-symmetric terephthalaldehydes respectively, including 2,5-dimethoxyterephthalaldehyde (PDA-OMe), 2,5-dihydroxyterephthalaldehyde (PDA-OH), terephthalaldehyde (PDA-H), 2,5-dibromoterephthalaldehyde (PDA-Br) and 2,5-dichloroterephthalaldehyde (PDA-Cl) (Fig. 1).²⁵ The chemical composition of these COFs was identified using Fourier transform infrared (FT-IR) spectra, as shown in Fig. S1.† The characteristic peaks in the infrared spectrum of TTA-COF-R at 1600 cm⁻¹ correspond to C=N tensile vibration, indicating the successful synthesis of the imine bond. And the absence of characteristic peaks at 1700 cm⁻¹ corresponding to C=O tensile vibration indicates that the functionalized terephthalaldehyde monomer was completely consumed. Based on powder X-ray diffraction (PXRD) data, all 5 kinds of TTA-COFs displayed the same main diffractions at 2.8°, 4.8°, 5.8°, 7.5°

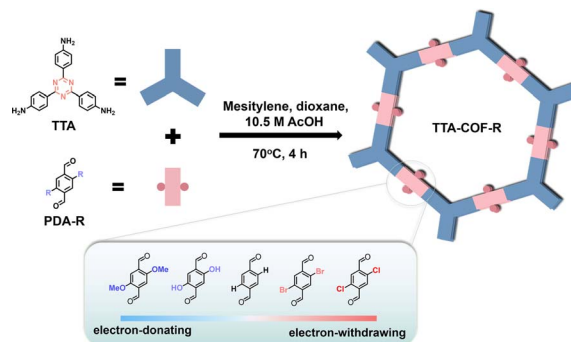


Fig. 1 Schematic illustration of the synthesis of TTA-COF-R.

and 25.5°, which can be assigned to the (100), (110), (200), (210) and (001) planes, respectively (Fig. 2a). These results are consistent with the theoretical prediction of the eclipsed AA layer stacking model, demonstrating that the modification of functional groups in terephthalaldehyde monomers did not affect the formation of COF crystal structures.²⁶ The porosity of these TTA-COF-R was characterized by nitrogen sorption measurements at 77 K. All the isotherm maps of TTA-COF-R were identified as type-IV isotherms with sharp N₂ uptakes at relative pressure $P/P_0 \leq 0.2$, indicating the existence of a mesoporous structure (Fig. 2b). The Brunauer–Emmett–Teller (BET) surface areas of TTA-COF-R exhibited largish surface areas, which were larger than >700 m² g⁻¹. The pore size distribution diagrams for TTA-COF-R were centred at about 2.0 nm and the pore volumes of TTA-COF-R (R = OMe, OH, H, Br, Cl) were calculated to be 1.30, 1.40, 0.43, 1.35 and 1.02 cm³ g⁻¹, respectively (Fig. 2c). Field emission scanning electron microscopy (FE-SEM) shows that the morphology of all materials is strip-shaped (Fig. S2†).

The optical absorption of TTA-COF-R was analysed to understand how the functional group modification changed photophysical properties. The UV-Vis diffuse reflectance spectra (UV-Vis DRS) of TTA-COF-R are as shown in Fig. 2d. The replacement of H atoms by different functional groups changed the composition and the band edge of the samples, resulting in enhanced visible absorbance. It is noteworthy that TTA-COF-OH increased the conjugation degree due to intramolecular hydrogen bonds and improved the flatness of two-dimensional layers, which resulted in the red shift of absorption edges.²⁷ The optical bandgap (E_g) was estimated according to the Kubelka–Munk function equation to be around 2.50 eV for TTA-COF-OMe, 2.25 eV for TTA-COF-OH, 2.72 eV for TTA-COF-H, 2.65 eV for TTA-COF-Br and 2.64 eV for TTA-COF-Cl (Fig. 2e). The introduction of functional groups narrowed the band gap of the material, indicating that less energy was required to excite carriers. Mott–Schottky (M–S) analysis was carried out to study energy band structures of TTA-COF-R. The positive slope of the tangent of M–S indicates that these materials are n-type organic semiconductors (Fig. S3†).

As shown by the energy band structure diagram, the conduction band potentials of all materials are more negative than the redox potential of O₂/O₂⁻ (-0.33 V vs. NHE), which

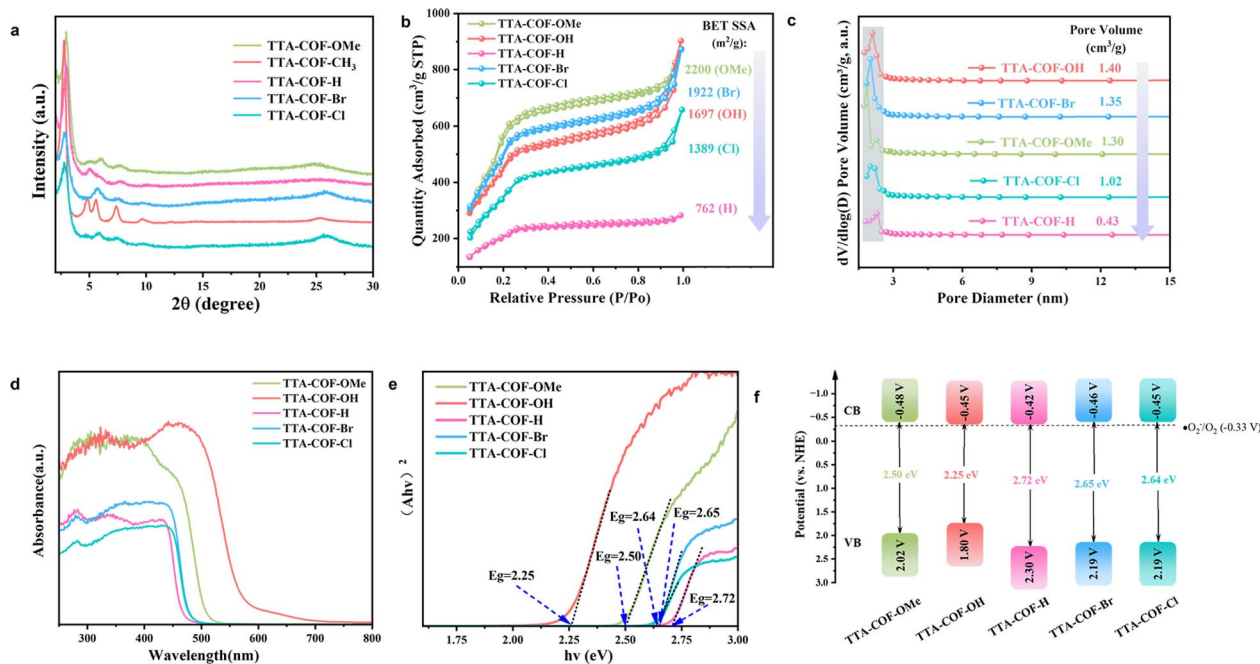


Fig. 2 (a) PXRD patterns of TTA-COF-R. (b) Nitrogen-sorption isotherms measured at 77 K and (c) pore size distribution profiles of TTA-COF-R. (d) UV-Vis DRS of TTA-COF-R. (e) The tauc plots of TTA-COF-R. (f) The band structure diagram of TTA-COF-R.

enables them to generate photoelectrons with strong reduction potential and ultimately produce $\cdot\text{O}_2^-$ (Fig. 2f). This indicates great potential for the photo-oxidation reduction reaction.

Photocatalytic performance of COFs

The photocatalytic performance of TTA-COF-R was evaluated by the Aza-Henry reaction mediated by the superoxide anion.^{28–31} We chose the reaction between **1a** and **2a** as a model reaction study under various reaction conditions. The representative results from this study are summarized in Tables S1–S4.† When the reaction between **1a** (1 equiv.) and **2a** (3 equiv.) was investigated by using 4 mg of TTA-COF-Br as a photocatalyst in MeOH (0.1 M) under O_2 and blue light irradiation for 1 h (Fig. 3a), it led to the formation of **3a** in the highest yield 79%. Negative-control experiments demonstrated that photocatalyst TTA-COF-R, light and oxygen are necessary (Table S1,† entries 2–5). In addition, the reaction with other solvents, such as toluene, acetone, acetonitrile, and cyclohexane, instead of MeOH was less efficient and resulted the product **3a** in less than 61% yield (Table S2†). Interestingly, performing the reaction with 2 mg of photocatalyst furnished **3a** in 16% yield, but when increasing the amount of photocatalyst from 4 mg to 6 mg, gave the product only in 62% yields (Table S3†). Finally, decreasing the amount of CH_3NO_2 **2a** from 3 equiv. to 2 equiv. furnished the product **3a** in only 46% yield (Table S4†). When TTA-COF-Cl, TTA-COF-H, TTA-COF-OMe and TTA-COF-OH were used instead of TTA-COF-Br as photocatalysts, they only led to 52%, 45%, 15% and 10% yield, respectively (Fig. 3b). Interestingly, the reaction rates varied significantly for TTA-COF-R according to their functional groups (–R). The initial reaction rate followed the order of TTA-COF-Br (1.25 Mm min^{-1}) > TTA-COF-Cl (1.17

Mm min^{-1}) > TTA-COF-H (1.12 Mm min^{-1}) > TTA-COF-OMe (0.27 Mm min^{-1}) > TTA-COF-OH (0.14 Mm min^{-1}) (Fig. 3c, S4†). The initial reaction rate of TTA-COF-Br was about 8 times that of TTA-COF-OH. Although at this stage we do not have any explanation, we can speculate that the electron-withdrawing group was beneficial for the oxidation reaction, while the electron-donating group hindered the reactivity of the oxidation reaction.

With the encouraging results, we investigated next the scope and limitations for this oxidase process by various nucleophiles as well as *N*-phenyl-1,2,3,4-tetrahydroisoquinoline derivatives (Fig. 3d). The oxidation reaction between **1a** with various nucleophiles (such as nitromethane, diethyl malonate, diethyl phosphite and acetone³¹) (**2a–2d**) has been successful, furnishing **3a–3d** in 79–96% yields. The oxidation reaction between nucleophiles (**2b–d**) with *N*-phenyl-1,2,3,4-tetrahydroisoquinoline derivatives bearing various functional groups (–OMe and –Br) (**1b** and **1c**) has been successfully achieved under a blue LED to afford the corresponding products (**3e–g**) in yields up to 97%. As a heterogeneous catalyst, it is very necessary to explore the reusable ability of the TTA-COF-Br catalyst for potential industrial application. Therefore, a recyclability test and hot filtration experiment were carried out (Fig. S5a and b†). The result indicates that the activity decreased slightly after five cycles. The PXRD pattern (Fig. S5c†) and UV-Vis DRS spectrum (Fig. S5d†) of the recycled TTA-COF-Br catalyst confirm that the crystallinity and the absorption range of TTA-COF-Br were almost maintained, although the intensity of the PXRD pattern was obviously decreased. To verify that this reaction cannot be catalysed by the monomers produced by decomposition of TTA-COF-Br, the hot filtration experiment was

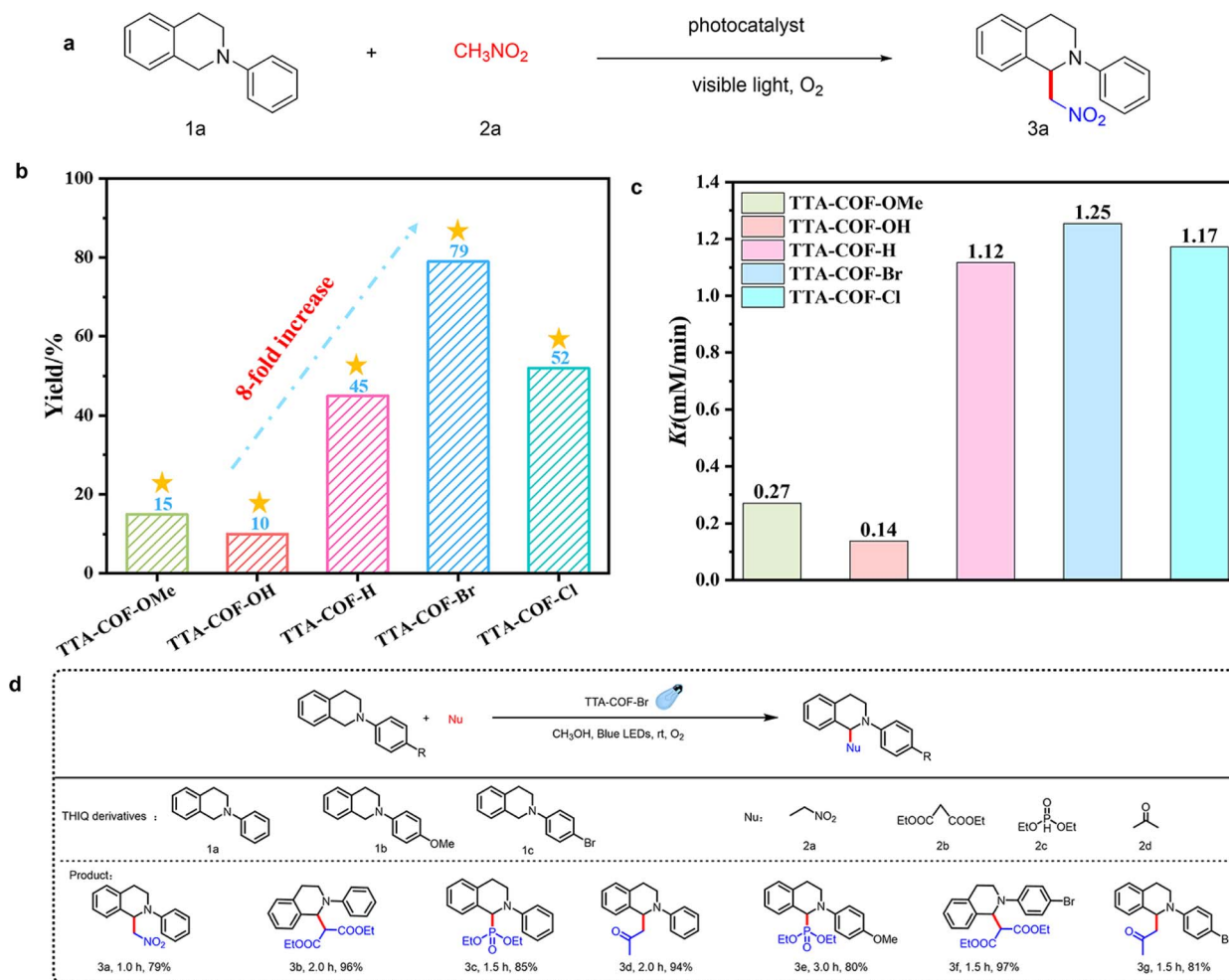


Fig. 3 (a) The template reaction of the Aza-Henry reaction. (b) Plots of **3a** vs. time from initial rate measurement for TTA-COF-R. (c) The initial reaction rate of TTA-COF-R. (d) Reaction scope of the Aza-Henry reaction catalyzed by TTA-COF-Br; the yield is isolated yield. (Reaction conditions: **1a** (0.2 mmol), **2a** (3.0 eq.) TTA-Br-COF (4 mg), methanol (2.0 mL), 25 °C, O₂ balloon, blue LED. The yield was calculated by HPLC after the reaction liquid extraction.)

conducted (Fig. S5b[†]), and the reaction did not exhibit any further reactivity after TTA-COF-Br was removed from the solution.

Mechanism research

To identify the active species of the reaction, trapping experiments were conducted by employing **1a** and **2a** as the reactants. As shown in Fig. 4a, *p*-benzoquinone (BQ), triethanolamine (TEOA), catalase (CAT), isopropanol (IP) and *L*-histidine were used as scavengers for the superoxide radical ([•]O₂⁻), hole (h⁺), H₂O₂, the hydroxyl radical ([•]OH) and singlet oxygen (¹O₂), respectively. When BQ was introduced, it was noticed that the reaction activity dramatically decreased. Similarly, the addition of TEOA to the system led to a lower product yield. And when CAT, IP and *L*-histidine were added to the best conditions, the yields did not change much. Those results fully demonstrated that the superoxide radical ([•]O₂⁻), which was generated by the photocatalysts TTA-COF-R, played a primary role in the Aza-Henry reaction. The hole was another important factor, which

supports our hypothesis that TTA-COF-OH, with the most positive VB edge potential, had the lowest activity. Furthermore, electron paramagnetic resonance (EPR) spin trapping experiments were used to detect the generated superoxide radical (Fig. 4b). After irradiating the mixture of 0.20 mmol **1a**, 4 mg TTA-COF-Br, 2 mL methanol and 5,5-dimethyl-1-pyrroline *N*-oxide (radical trapping reagent) with blue light, the typical characteristic signal of [•]O₂⁻ was observed by the EPR experiment. And the generation of superoxide radicals in the five COFs under photocatalytic conditions was further validated by the typical reaction with nitrotetrazolium blue chloride (NBT) (Fig. S6[†]).³²

The generation of the superoxide radical ([•]O₂⁻) in the five photocatalytic systems followed the order of TTA-COF-Br > TTA-COF-Cl > TTA-COF-OH > TTA-COF-H > TTA-COF-OMe, which was consistent with the performance of the photocatalytic Aza-Henry reaction, except for TTA-COF-OH (Fig. 4c). Because the detection was performed in water, TTA-COF-OH exhibited enol-ketone tautomerism, increasing its electron-absorbing capabilities and

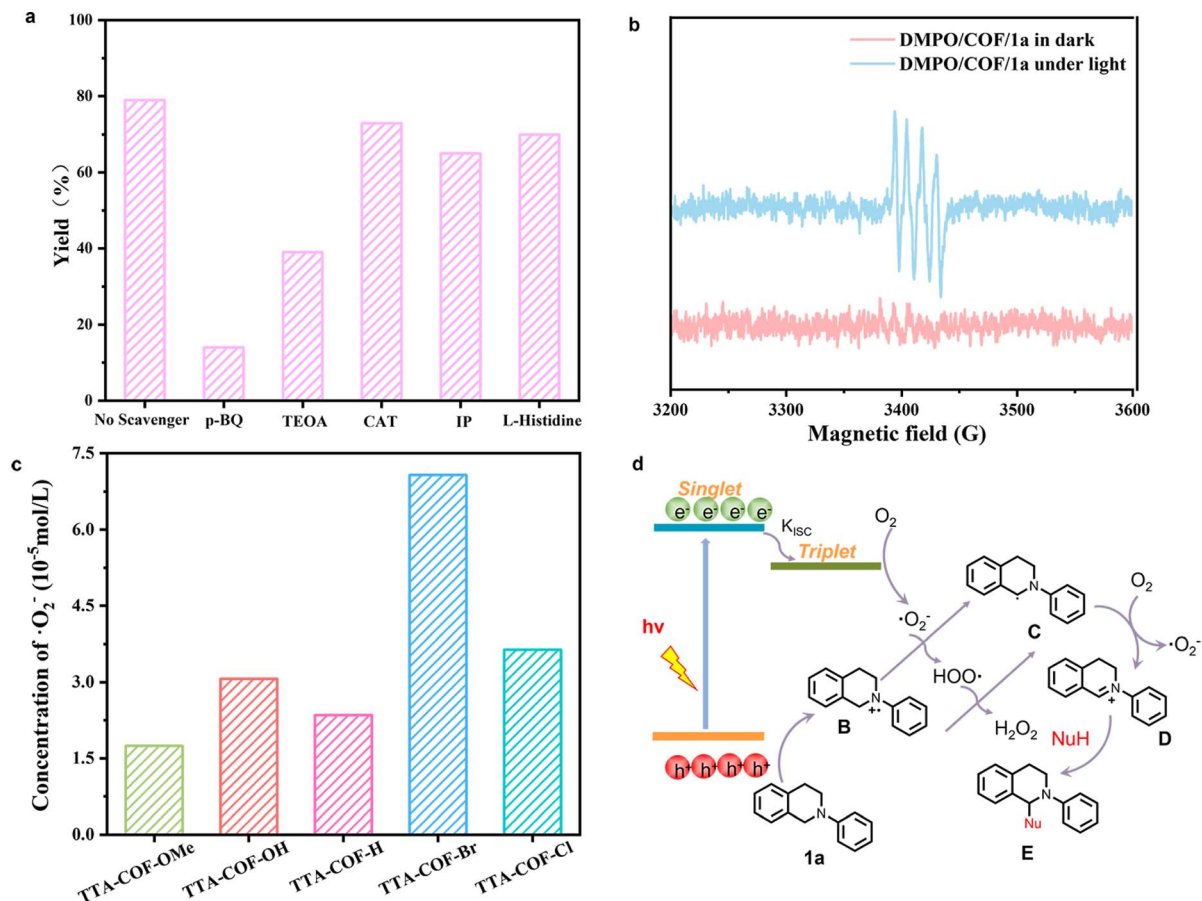


Fig. 4 (a) The free-radical-capture experiments. (b) The EPR spectra of DMPO- $\cdot\text{O}_2^-$ over TTA-COF-Br under blue LED irradiation. (c) The generation of $\cdot\text{O}_2^-$ in the visible-light photocatalytic systems catalyzed by TTA-COF-R. (d) Proposed mechanistic pathway of the Aza-Henry reaction.

promoting charge separation.³³ Therefore, a reasonable reaction mechanism (Fig. 4d) is proposed. Under the irradiation of visible light, the COF is excited to produce electron-hole pairs. Tetrahydroisoquinoline **1a** was oxidized by holes to produce free radical cation **B**. Electrons reduce oxygen to a superoxide anion, which then abstracts a hydrogen atom from free radical cation **B**, yielding the **C** radical and $\text{HOO}\cdot$. Free radical **C** can also be produced by the reaction between **A** and $\text{HOO}\cdot$, which leads to the formation of hydrogen peroxide. The formation of hydrogen peroxide in our system was evidenced in the ^1H NMR spectrum (Fig. S7†). The imine intermediate **D** is then produced by the electron loss of radical **C**. Finally, the nucleophilic addition of the nucleophilic reagent and **D** affords the desired product **E**.

The investigation of key factors for photocatalytic performance

To prioritize the key factors for efficient Aza-Henry reaction, we analyzed the correlation between the photocatalytic activity of all the COFs and the BET surface area, band gap, valence band and driving force for oxygen reduction in the following section (Table 1). TTA-COF-OH has the narrowest band gap, but it also shows the lowest photocatalytic activity, suggesting that the band gap is not the main factor in photooxidation.

The BET surface area of TTA-COF-H is smaller than that of TTA-COF-OMe and TTA-COF-OH, but its activity is higher, indicating that BET surface area does not determine the photocatalytic performance.³⁴

TTA-COF-OMe has larger specific surface area, higher oxygen reduction driving force and a smaller band gap than TTA-COF-Br, but its activity is lower than that of TTA-COF-Br, which might be attributed to the more positive valence band value of TTA-COF-OMe than that of TTA-COF-Br. TTA-COF-Br and TTA-COF-Cl have similar energy band structures, but the activity of TTA-COF-Br is 1.5 times that of TTA-COF-Cl. In this case, better charge carrier generation and transport may play a significant role in this reaction.

To support the above-mentioned notion, we investigated the photoelectric properties of TTA-COF-R by transient photocurrent and electrochemical impedance spectroscopy (EIS). As shown in Fig. 5a, the transient photocurrent-time ($i-t$) curve of COFs was recorded using on-off cycles of intermittent irradiation under a blue LED (450 nm). The strength of the transient photocurrent response followed the order of TTA-COF-Br > TTA-COF-Cl > TTA-COF-H > TTA-COF-OH > TTA-COF-OMe. A higher photocurrent indicates that photo-excited electron-hole pairs can be separated more effectively and thus more photoelectrons

Table 1 Surface area, band structure, and photocatalytic performance of the COFs

COF	BET surface area ($\text{m}^2 \text{g}^{-1}$)	Band gap (eV)	Valence band (V)	Driving force ^a (V)	3a yield (%)
TTA-COF-OMe	2200	2.50	2.02	-0.15	15
TTA-COF-OH	1697	2.25	1.80	-0.11	10
TTA-COF-H	762	2.72	2.30	-0.09	45
TTA-COF-Br	1922	2.65	2.19	-0.13	79
TTA-COF-Cl	1389	2.64	2.19	-0.12	52

^a Driving force for oxygen reduction = (CBM - (-0.33 V vs. NHE, potential of O_2/O_2^-)) at pH 7.

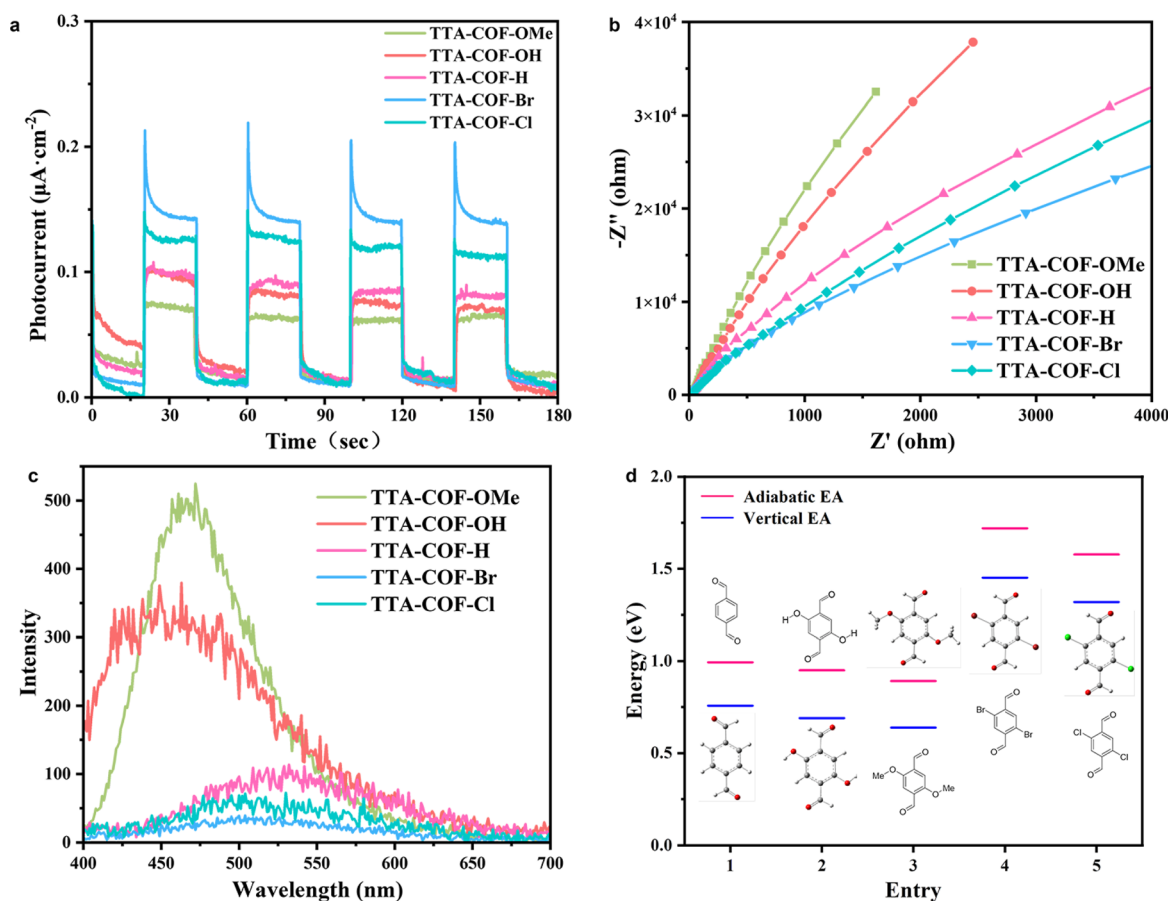


Fig. 5 (a) Transient photocurrent responses. (b) Electrochemical impedance spectroscopy and (c) PL spectra (excitation wavelength = 365 nm) of the COFs. (d) Calculated electron affinities of the aldehyde monomer. Calculated at the B3LYP/6-31G(d,p) level in the gas phase.

are available for photocatalytic conversion. Next, we used the electrochemical impedance spectroscopy (EIS) Nyquist diagram to further characterize the resistance during interfacial charge transfer. Fig. 5b shows that the radius of the Nyquist plot followed the order of TTA-COF-Br < TTA-COF-Cl < TTA-COF-H < TTA-COF-OH < TTA-COF-OMe, which reveals that TTA-COF-Br had better conductivity and a faster electron transfer rate. Obviously, bromine atoms endowed TTA-COF-Br with excellent photoelectric properties in photocatalytic applications, especially enhancing the efficiency of charge generation and transfer to promote the activation of molecular oxygen. Furthermore, we observed the same trend in the photoluminescence (PL) spectra

(Fig. 5c). The recombination of dispersed photo-generated carriers (holes and electrons) was inhibited with decreasing emission peaks. These photoelectric characterization studies demonstrate why TTA-COF-Br has a higher catalytic activity than other TTA-COFs.

To further unravel the influence of substituent group modulation on the photocatalytic Aza-Henry reaction of TTA-COF-R, density functional theory (DFT) calculations were carried out. Compared with COFs, which have a complex structure and are challenging to compute, organic molecular monomers have become a popular option for research because of their clear molecular structure and composition.³⁵ The

macro-properties of COFs are determined by the microstructures of the monomers. To understand the relationship between functional group substituents and photocatalytic activity, we need to know the energy band structure of the underlying building blocks. As shown in Fig. S8,[†] E_g is the energy level difference between the highest occupied molecular orbital (HOMO) and lowest unoccupied molecular orbital (LUMO), E_{opt} is the optical band gap, and E_b is the exciton binding energy. The dissociation of excitons and the efficient separation of hole–electron pairs are more advantageous for smaller E_b values. For conjugated molecules, the E_b decreases with an increase in electronic affinity (EA).³⁶

Therefore, the EAs of PDA-R (R = H, OH, OMe, Br, Cl) were calculated (Fig. 5d, Table S5[†]). Higher EA is associated with higher charge separation efficiency and increased stability in the structure while receiving additional electrons.³⁷ The EA values follow the order of PDA-Br > PDA-Cl > PDA-OH > PDA-H > PDA-OMe, which is consistent with most of the experimental results. However, there is an unmatched result between the calculation results and the experiments, in which COF-OMe has a better catalytic performance than COF-OH. This is because the calculation does not take into account the overall structure of COFs and the model PDA-OH used in the calculation is an aldehyde-based structural unit with hydrogen bonds, which may deviate from the actual situation.³⁸ Moreover, although the ideal arrangement of building blocks for a successful charge separation is not precisely proportionate, the correlation

between their exciton binding energy and EA may be informative enough to identify an ideal configuration.³⁹

Verification of structure–activity relationship

To further demonstrate that the structure–activity relationship of materials is universal, another set of TAPB-COF-R (R = OMe, OH, H, Br, Cl) was synthesized by replacing TTA with TAPB (Fig. S9[†]). PXRD, FT-IR spectra and nitrogen-sorption isotherm measurements confirmed the successful preparation of the materials (Fig. 6a, S10 and S11[†]). As shown in Fig. 6b and c, the absorption range of TAPB-COF-R was wider and the band gap was narrower than those of TAPB-COF-H. And the band gap energy followed the order of TAPB-COF-OH < TAPB-COF-OMe < TAPB-COF-Br < TAPB-COF-Cl < TAPB-COF-H, consistent with TTA-COF-R. The energy levels of the five materials were calculated by Mott–Schottky measurements (Fig. S12[†]). Conduction band potentials of the five TAPB-COF-R were more negative than the redox potential of O_2/O_2^- (−0.33 V vs. NHE), indicating that the Aza–Henry reaction could also occur (Fig. 6d).

Next, we tested the photocatalytic Aza–Henry reaction activity of all of the TAPB-COF-R under the optimal conditions. Fig. 6e shows the activity performance of the product **3a** during a 1.0 h test period. The activity performance followed the same order of TAPB-COF-OH < TAPB-COF-OMe < TAPB-COF-H < TAPB-COF-Cl < TAPB-COF-Br with TTA-COF-R. Compared to TAPB, TAA exhibits higher absorbance and red-shifted absorption in UV-Vis spectroscopy, indicating a stronger absorption

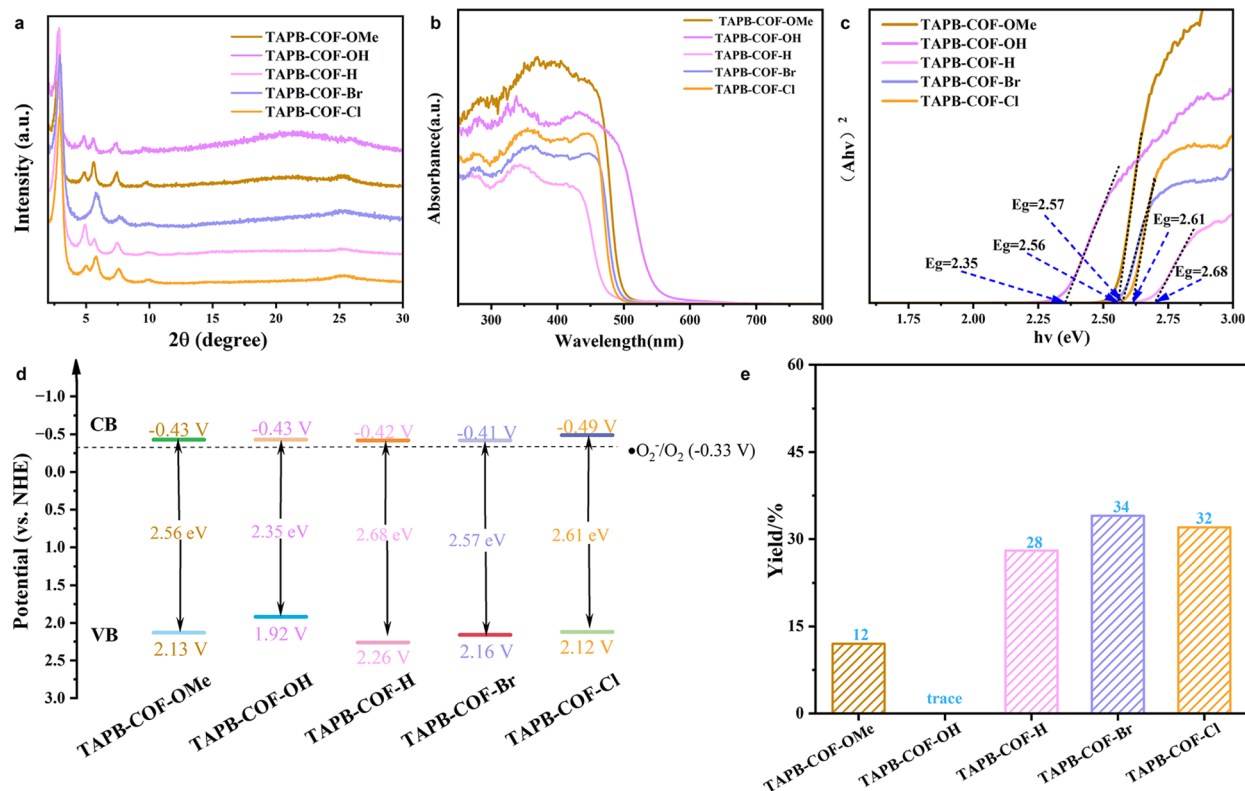


Fig. 6 (a) PXRD patterns of TAPB-COF-R. (b) UV-Vis DRS of TAPB-COF-R. (c) The tauc plots of TAPB-COF-R. (d) The band structure diagram of TAPB-COF-R. (e) Comparison of catalyst performance of TAPB-COF-R.

capability for visible light (Fig. S13a†). The TTA monomer has a larger planarity compared to the TAPB monomer (Fig. S13b†), resulting in increased planarity of the framework, which augments the efficiency of charge transfer and separation.^{40,41}

What's more, TTA-COF-Br shows stronger photocurrent response and smaller impedance than TAPB-COF-Br by electrochemical characterization (Fig. S13c and d†). Therefore, considering factors such as absorbance, charge separation efficiency, and photocurrent, it is demonstrated that TTA-COF-Br exhibits higher photocatalytic activity compared to TAPB-COF-Br. These results verify that the introduction of substituents affected the activity of the oxidase reaction and that electron-withdrawing substituents promoted the activity of photocatalysts. Because the electron-withdrawing group has great electron affinity, it enhances the generation and intramolecular transfer of charge carriers, which is the decisive factor in photocatalytic reactions.⁴²

Conclusions

In summary, we explored the structure–property–activity relationship of ten kinds of COFs with similar topological structures and different functional groups, using the oxidase reaction as an experimental proof, photoelectric properties and DFT calculations as theoretical supports. By integrating the experimental proof and theoretical supports, we disclosed that the electron affinity of the substituents was the crucial factor influencing the oxidase reaction and properties of COFs. And we successfully revealed that the activity of the oxidase reaction was increased by doping the functional groups with high charge carrier generation and transport to COFs, such as electron-withdrawing groups. This work not only provides an exciting new perspective and opportunity for studying the structure–activity relationship of polymer catalysts with the photochemical and electronic properties of small molecules and for guiding the design of high-performance photocatalysts, but also provides a novel theoretical base for machine learning in the chemistry area.

Experimental methods

Synthesis of COFs

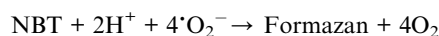
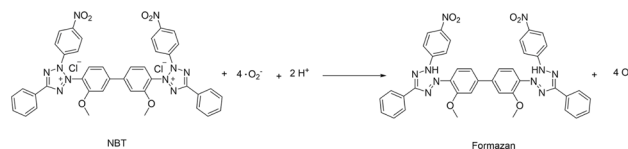
TAPB/TTA-COF-R were synthesized based on a recipe and procedure reported in the literature with some modifications.²⁵ Typically, TAPB or TTA (0.095 mmol) and PDA-R (0.143 mmol) are weighed into a vial. 1 mL of 4 : 1 1,4-dioxane : mesitylene was added to the vial, which was sonicated thoroughly (1–2 minutes). The vial was preheated to 70 °C and 0.5 mL of 10.5 M acetic acid was added. Then the reaction mixture was allowed to stand for 4 hours at 70 °C. The COF reaction mixture was washed with methanol and soaked with DCM. After 1 h, it was replaced with new DCM, and this process was repeated twice. Subsequently, the DCM was decanted and replaced with *n*-hexane. At an interval of 1 h, *n*-hexane was replaced with fresh solvent three times. *N*-hexane was removed and activated at 150 °C by a nitrogen flow for 3 h.

A general procedure for the Aza–Henry reaction of tetrahydroisoquinolines

In a typical experiment, tetrahydroisoquinoline derivatives (0.2 mmol), nitromethane (0.6 mmol), TTA/TAPB-COF-R (4.0 mg) and methanol (2.0 mL) were mixed and added in a quartz vial with a magnetic stirring bar. Subsequently, the mixture was sonicated and stirred for 20 minutes. After that, the mixture was bubbled with an oxygen stream for 5 minutes and an oxygen ball was added. Then, it was irradiated using a 30 W blue LED lamp under rapid stirring for 1.5 h at 25 °C. Finally, the reaction mixture was filtered, the organic phase was diluted with methanol, and the volume was fixed in a 1.0 mL bottle. The sample was analyzed using an Agilent 1260 Series Triple Quad high-performance liquid chromatography (HPLC) system with an Agilent C18 reverse-phase chromatographic column. The conversion of tetrahydroisoquinolines and the yield of the product were determined by using naphthalene as the internal standard. All data were obtained at least twice, and the data error was ensured to be within ±5%.

The quantitative calculation of superoxide radical generation by NBT

The concentration of $\cdot\text{O}_2^-$ was measured by detecting the decay of NBT (nitro blue tetrazolium) using UV-Vis spectroscopy.³² 3 mL of liquid was filtered with a 0.22 μm filter to remove the photocatalysts. The photocatalytic generation of $\cdot\text{O}_2^-$ was determined by the degradation of NBT, which was detected by the absorbance change at a wavelength of 259 nm. The mole ratio of generated $\cdot\text{O}_2^-$ and reacted NBT was 4 : 1 according to the following equation:



$$n(\cdot\text{O}_2^-) = (1 - \text{NBT}_t / \text{NBT}_0) \times 4$$

Calculation method

The Gaussian 16 (ref. 43) package was used to obtain the electron affinity of the linkers. Becke's 3-parameter nonlocal exchange and functional Lee–Yang–Parr nonlocal correlation (B3LYP^{44–47}) functional and the 6-31G(d,p) basis set were used. All geometries are optimized before further electronic properties are calculated. The “g09defaults” keyword was used in all calculations to save computational costs. Vibrational analysis was performed for all optimized geometries to confirm that there is no imaginary frequency. Electron affinity (EA) was calculated using the following equation:

$$\text{EA} = E(\text{M}) - E(\text{M}^-)$$

where $E(M)$ and $E(M^-)$ are the neutral and anionic energies, respectively. $E(M^-)$ is the anionic energy of the optimized neutral structure in vertical EA and the energy of the optimized anionic structures in adiabatic EA.

Author contributions

Huiying Chen: conceptualization, methodology, validation, investigation, writing – original draft. Qinghai Zhou: software, methodology, data curation, validation. Jinyang Hai: investigation, data curation. Mingxiang Zhu: conceptualization, methodology, supervision, writing – review & editing. Fang Zhang: conceptualization, funding acquisition, methodology, project administration, supervision, writing – review & editing.

Conflicts of interest

There are no conflicts to declare.

Acknowledgements

This work was supported by NSFC (22076122) and Shanghai Government (19SG42, 23010504000 and 22ZR1480200).

References

- 1 C. Ayed, J. Yin, K. Landfester and K. A. I. Zhang, *Angew. Chem., Int. Ed.*, 2023, e202216159.
- 2 N. L. Reed and T. P. Yoon, *Chem. Soc. Rev.*, 2021, **50**, 2954–2967.
- 3 A. G. Condie, J. C. González-Gómez and C. R. J. Stephenson, *J. Am. Chem. Soc.*, 2010, **132**, 1464–1465.
- 4 A. M. Pembere and Z. Luo, *Phys. Chem. Chem. Phys.*, 2017, **19**, 6620–6625.
- 5 V. Hardouin Duparc, G. L. Bano and F. Schaper, *ACS Catal.*, 2018, **8**, 7308–7325.
- 6 Z. T. Pan, L. M. Shen, F. W. Dagnaw, J. J. Zhong, J. X. Jian and Q. X. Tong, *Chem. Commun.*, 2023, **59**, 1637–1640.
- 7 W. Nam, Y. M. Lee and S. Fukuzumi, *Acc. Chem. Res.*, 2018, **51**, 2014–2022.
- 8 J. M. Anglada, M. Martins-Costa, J. S. Francisco and M. F. Ruiz-López, *Acc. Chem. Res.*, 2015, **48**, 575–583.
- 9 E. Romero, J. R. Gómez Castellanos, G. Gadda, M. W. Fraaije and A. Mattevi, *Chem. Rev.*, 2018, **118**, 1742–1769.
- 10 K. Qian, L. Du, X. Zhu, S. Liang, S. Chen, H. Kobayashi, X. Yan, M. Xu, Y. Dai and R. Li, *J. Mater. Chem. A*, 2019, **7**, 14592–14601.
- 11 Y. Chong, Q. Liu and C. Ge, *Nano Today*, 2021, **37**, 101076.
- 12 W. Jiang, X. An, J. Xiao, Z. Yang, J. Liu, H. Chen, H. Li, W. Zhu, H. Li and S. Dai, *ACS Catal.*, 2022, **12**, 8623–8631.
- 13 H. Wang, D. Yong, S. Chen, S. Jiang, X. Zhang, W. Shao, Q. Zhang, W. Yan, B. Pan and Y. Xie, *J. Am. Chem. Soc.*, 2018, **140**, 1760–1766.
- 14 Q. Wang, H. Zhou, X. Liu, T. Li, C. Jiang, W. Song and W. Chen, *Environ. Sci.: Nano*, 2018, **5**, 2864–2875.
- 15 Y. Nosaka and A. Y. Nosaka, *Chem. Rev.*, 2017, **117**, 11302–11336.
- 16 R. Das, C. D. Vecitis, A. Schulze, B. Cao, A. F. Ismail, X. Lu, J. Chen and S. Ramakrishna, *Chem. Soc. Rev.*, 2017, **46**, 6946–7020.
- 17 T. Zhou, L. Wang, X. Huang, J. Unruangsri, H. Zhang, R. Wang, Q. Song, Q. Yang, W. Li, C. Wang, K. Takahashi, H. Xu and J. Guo, *Nat. Commun.*, 2021, **12**, 3934.
- 18 X. Li, C. Zhang, S. Cai, X. Lei, V. Altoe, F. Hong, J. J. Urban, J. Ciston, E. M. Chan and Y. Liu, *Nat. Commun.*, 2018, **9**, 2998.
- 19 L. Zhang, X. Zhang, D. Han, L. Zhai and L. Mi, *Small Methods*, 2023, **7**, 2300687.
- 20 Z. Liang, R. Shen, Y. H. Ng, Y. Fu, T. Ma, P. Zhang, Y. Li and X. Li, *Chem Catal.*, 2022, **2**, 2157–2228.
- 21 Z. Li, T. Deng, S. Ma, Z. Zhang, G. Wu, J. Wang, Q. Li, H. Xia, S. W. Yang and X. Liu, *J. Am. Chem. Soc.*, 2023, **145**, 8364–8374.
- 22 F. Yang, C. C. Li, C. C. Xu, J. L. Kan, B. Tian, H. Y. Qu, Y. Guo, Y. Geng and Y. B. Dong, *Chem. Commun.*, 2022, **58**, 1530–1533.
- 23 K. Xiong, Y. Wang, F. Zhang, X. Li and X. Lang, *Appl. Catal., B*, 2023, **322**, 122135.
- 24 J. L. Shi, R. Chen, H. Hao, C. Wang and X. Lang, *Angew. Chem., Int. Ed.*, 2020, **59**, 9088–9093.
- 25 C. H. Feriante, S. Jhulki, A. M. Evans, R. R. Dasari, K. Slicker, W. R. Dichtel and S. R. Marder, *Adv. Mater.*, 2020, **32**, e1905776.
- 26 C. Kang, K. Yang, Z. Zhang, A. K. Usadi, D. C. Calabro, L. S. Baugh, Y. Wang, J. Jiang, X. Zou, Z. Huang and D. Zhao, *Nat. Commun.*, 2022, **13**, 1370.
- 27 J. Yang, F. Kang, X. Wang and Q. Zhang, *Mater. Horiz.*, 2022, **9**, 121–146.
- 28 Y. Zhi, Z. Li, X. Feng, H. Xia, Y. Zhang, Z. Shi, Y. Mu and X. Liu, *J. Mater. Chem. A*, 2017, **5**, 22933–22938.
- 29 Y. Kim and C.-J. Li, *Green Synth. Catal.*, 2020, **1**, 1–11.
- 30 A. K. Bagdi, M. Rahman, D. Bhattacharjee, G. V. Zyryanov, S. Ghosh, O. N. Chupakhin and A. Hajra, *Green Chem.*, 2020, **22**, 6632–6681.
- 31 M. Rueping, C. Vila, R. M. Koenigs, K. Poschary and D. C. Fabry, *Chem. Commun.*, 2011, **47**, 2360–2362.
- 32 H. Wang, C. Yang, F. Chen, G. Zheng and Q. Han, *Angew. Chem., Int. Ed.*, 2022, **61**, e202202328.
- 33 X. Li, Q. Gao, J. Aneesh, H.-S. Xu, Z. Chen, W. Tang, C. Liu, X. Shi, K. V. Adarsh, Y. Lu and K. P. Loh, *Chem. Mater.*, 2018, **30**, 5743–5749.
- 34 J. Liu, S. Zhang and H. Zhao, *Appl. Surf. Sci.*, 2019, **479**, 247–252.
- 35 X. Li, P. M. Maffettone, Y. Che, T. Liu, L. Chen and A. I. Cooper, *Chem. Sci.*, 2021, **12**, 10742–10754.
- 36 J. P. Jeon, Y. J. Kim, S. H. Joo, H. J. Noh, S. K. Kwak and J. B. Baek, *Angew. Chem., Int. Ed.*, 2022, e202217416.
- 37 G. Gogoi, L. Bhattacharya, S. Rahman, N. S. Sarma, S. Sahu, B. K. Rajbongshi and S. Sharma, *Mater. Today Commun.*, 2020, **25**, 101364.
- 38 S. Ghosh, A. Nakada, M. A. Springer, T. Kawaguchi, K. Suzuki, H. Kaji, I. Baburin, A. Kuc, T. Heine, H. Suzuki, R. Abe and S. Seki, *J. Am. Chem. Soc.*, 2020, **142**, 9752–9762.

- 39 P. J. Leenaers, A. J. L. A. Maufort, M. M. Wienk and R. A. J. Janssen, *J. Phys. Chem. C*, 2020, **124**, 27403–27412.
- 40 A. F. M. El-Mahdy, C.-H. Kuo, A. Alshehri, C. Young, Y. Yamauchi, J. Kim and S.-W. Kuo, *J. Mater. Chem. A*, 2018, **6**, 19532–19541.
- 41 H. So, J. H. Kim, J. H. Lee, H. Hwang, D. K. An and K. M. Lee, *Chem. Commun.*, 2019, **55**, 14518–14521.
- 42 L. Ma, H. Yao, J. Wang, Y. Xu, M. Gao, Y. Zu, Y. Cui, S. Zhang, L. Ye and J. Hou, *Angew. Chem., Int. Ed.*, 2021, **60**, 15988–15994.
- 43 M. J. Frisch, G. W. Trucks, H. B. Schlegel, G. E. Scuseria, M. A. Robb, J. R. Cheeseman, G. Scalmani, V. Barone, G. A. Petersson, H. Nakatsuji, X. Li, M. Caricato, A. V. Marenich, J. Bloino, B. G. Janesko, R. Gomperts, B. Mennucci, H. P. Hratchian, J. V. Ortiz, A. F. Izmaylov, J. L. Sonnenberg, D. Williams-Young, F. Ding, F. Lipparini, F. Egidi, J. Goings, B. Peng, A. Petrone, T. Henderson, D. Ranasinghe, V. G. Zakrzewski, J. Gao, N. Rega, G. Zheng, W. Liang, M. Hada, M. Ehara, K. Toyota, R. Fukuda, J. Hasegawa, M. Ishida, T. Nakajima, Y. Honda, O. Kitao, H. Nakai, T. Vreven, K. Throssell, J. A. Montgomery Jr., J. E. Peralta, F. Ogliaro, M. J. Bearpark, J. J. Heyd, E. N. Brothers, K. N. Kudin, V. N. Staroverov, T. A. Keith, R. Kobayashi, J. Normand, K. Raghavachari, A. P. Rendell, J. C. Burant, S. S. Iyengar, J. Tomasi, M. Cossi, J. M. Millam, M. Klene, C. Adamo, R. Cammi, J. W. Ochterski, R. L. Martin, K. Morokuma, O. Farkas, J. B. Foresman and D. J. Fox, *Gaussian 16 Rev. B.01*, Wallingford, CT, 2016.
- 44 A. D. Becke, *J. Chem. Phys.*, 1993, **98**, 5648–5652.
- 45 C. Lee, W. Yang and R. G. Parr, *Phys. Rev. B: Condens. Matter Mater. Phys.*, 1988, **37**, 785–789.
- 46 S. H. Vosko, L. Wilk and M. Nusair, *Can. J. Phys.*, 1980, **58**, 1200–1211.
- 47 J. Tirado-Rives and W. L. Jorgensen, *J. Chem. Theory Comput.*, 2008, **4**, 297–306.